

An effective curved space-time geometric theory of generic twist angle graphene with application to a rotating bilayer configuration

Jia-Zheng Ma¹, Trinanjan Datta^{2,*} and Dao-Xin Yao^{1†}

¹*State Key Laboratory of Optoelectronic Materials and Technologies,
School of Physics, Sun Yat-Sen University, Guangzhou 510275, China*

²*Department of Chemistry and Physics, Augusta University, 1120 15th Street, Augusta, Georgia 30912, USA*

(Dated: November 15, 2021)

We propose a new kind of geometric effective theory based on curved space-time single valley Dirac theory with spin connection for twisted bilayer graphene under generic twist angle. This model can reproduce the nearly flat bands with particle-hole symmetry around the first magic angle. The band width is near the former results given by Bistritzer-MacDonald model or density matrix renormalization group. Even more, such geometric formalism allows one to predict the properties of rotating bilayer graphene which cannot be accessed by former theories. As an example, we investigate the Bott index of a rotating bilayer graphene. We relate this to the two-dimensional Thouless pump with quantized charge pumping during one driving period which could be verified by transport measurement.

I. INTRODUCTION

Twisted bilayer graphene (TBG) has attracted great interest both from a theoretical [1] and an experimental perspective [2, 3]. This system, which is rich in its physical behavior, provides a platform for studying the strongly correlated electronic state [2], orbital magnetism [4, 5], superconductivity [3] fragile topological phase [6, 7], higher-order topological insulator phase [8] and higher-order topological superconductivity [9]. Furthermore, heterostructure based on TBG may have potential application in superconducting devices [10] and quantum computation [11]. While several theories have been proposed to explain the occurrence of electronic phases in TBG, amongst them, the Bistritzer–MacDonald (BM) model and its descendants [12–14] have been successful in explaining electron localization near the magic angle. The BM model is valid only for small twist angle as it needs to ensure approximate translation symmetry for constructing a momentum space effective theory. A real space effective field theory formalism of TBG, limited to small deformation gradient has also been constructed [15]. Furthermore, the curved space quantum field theory (QFT) formalism has been utilized to explain the magic continuum within the context of staggered flux twisted bilayer square lattice [16]. However, a real space field theory formalism for generic twist angle in a moiré system is still missing. Thus, there is a need for a generic twist angle theory for TBG and twisted bilayer bravais lattice [17].

The need for the generic twist angle theory becomes apparent if we consider an out of equilibrium system. In this context, optical Floquet engineering [18, 19] and the Thouless pump [20] physics of TBG have been studied. Since a theory based on commensurate approximation [21] is not enough to capture the incommensurate nature for any twisted angle, there is a need to develop a geometric theory for generic twisted angle. Such a formalism can be applied to non-adiabatic rotation, including a structurally rotating TBG

which we call the rotating bilayer graphene (RBG).

In this article we have obtained the deformation field under an arbitrary twist angle and the energy bands at the first magic angle based on curved space-time Dirac action for a non-interacting TBG and RBG model. We utilize a geometric method to study the physics of TBG. This method is in principle valid for arbitrary twist angle, which is mainly inspired by considering the twist as a kind of deformation [15] and attributing the approximate zero energy flat band to the effective SU(2) gauge field (pseudo magnetic vector potential) in TBG [12, 16, 22–25]. Such a geometric theory can be naturally generalized to the case of a RBG system, which cannot be modeled by previous theoretical formulations. By calculating the Bott index, we obtain the quantized charge pumping in RBG. Within our effective geometric theory, the emergent SU(2) gauge field in RBG will generate a spin connection which will mix with the Aharonov-Anandan (AA) connection in RBG. The total connection will be the summation of these two components with AA connection and may give rise to new topological phases as well as new type of Floquet engineering in TBG (compared to Floquet engineering based on optical driving [18]). For simplicity, we consider a non-interacting model as a first attempt to generic TBG geometric formalism. The key point is to recover the flat bands and generalize to a RBG configuration.

This article is organized as follows. In Sec. II we briefly review the theoretical development of TBG. In Sec. III we show how to obtain the deformation field under arbitrary twist angle and the corresponding vierbein. In Sec. IV we solve the curved space Dirac equation at the first magic angle as a benchmark. In Sec. V we introduce the RBG model and compute the Bott index as an indicator of topological charge pumping. In Sec. VI we provide our conclusions and discussions. In Appendix A we show the non-hermiticity of curved space Dirac equation discretization. Finally, in Appendix B we provide details on the commutations of mixed second order derivative of the deformation field in RBG.

* tdatta@augusta.edu

† yaodaox@mail.sysu.edu.cn

II. A BRIEF REVIEW OF TWISTED BILAYER GRAPHENE

In this section we provide a brief review of the TBG focusing exclusively on theoretical and numerical developments. The first tight binding (non-interacting) model was proposed in Ref. 1. For small twisted angle, only three dominant momentum transfers were considered. The interlayer moiré modulated coupling was projected to momentum space and considered as a perturbation. Next, Guinea *et al.* showed that the moiré coupling in TBG can be regarded as a SU(2) gauge field which is responsible for band flattening in TBG [12]. Subsequently, all the magic angles and the analytic ground state wavefunction around magic angles were derived [13]. Furthermore, the magic angle was obtained by combining Wenzel-Kramers-Brillouin approximation (WKB) and asymptotic Airy function solution with single value condition [14]. Recently, several phenomenological many body interacting models for magic angle TBG (MATBG) considering long range Coulomb interaction have also been proposed. Ref [26] considers TBG as an extended Hubbard model on triangular superlattice. For MATBG, Jian Kang *et al.* has established a U(4) many body model [27]. Bernervig *et. al.* generalized the Kang-Vafek model with more exotic excitations via quantum geometric method [28]. Furthermore, several numerical methods have been developed to solve the TBG many body Hamiltonian including exact diagonalization (ED) [29], determinant quantum Monte Carlo (DQMC) [30, 31], dynamical mean field theory (DMFT) [32], density matrix renormalization group (DMRG) [33, 34]. Furthermore, a real space formalism has been developed regarding the twist as a special deformation [15]. This theory has the advantage of characterizing the effect of strain. Its descendant has been used in twisted bilayer staggered flux square lattice [16] (a model of twisted bilayer spin liquid) and explains the magic continuum. In addition to the above, Ref. 35 has proposed holographic duality construction of flat band and revealed the presence of nematic order. Furthermore, Ref. 36 based on fracton-elasticity duality has explained TBG quasicrystal elasticity. Ref. 37 implemented a geometric method based on Fubini-Study metric approach and deduced the Landau zero energy flat band with interaction in TBG. There has also been a calculation based on the vierbein formalism which demonstrates that there exists emergent moiré gravity in stained TBG [38].

III. THE VIERBEIN FORMALISM FOR TBG AND THE DEFORMATION FIELD

In this section we construct the vierbein formalism for the deformation field in TBG without strain, which implies no lattice relaxation and torsion. The necessity of introducing vierbein and curved space-time is to faithfully describe the geometric response of Dirac fermion in real space. Compared to the BM model, the vierbein formalism is applicable for generic twisted angle which may have no translation symmetry. When compared to the real space model formulation [15], the vierbein formalism can handle the system even with sin-

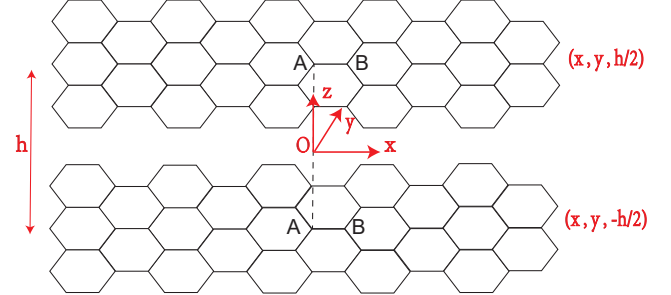


Figure 1. The coordinate notation scheme. The origin is the cross point of rotation axis and middle plane $z = 0$. Two layers lay in $z = \pm h/2$ respectively. The rotation axis goes through the sites of A sublattice from each layer for untwisted AA stacking bilayer graphene.

gular deformation field $|\partial_i \mathbf{u}| \gg 1$. Thus, the curved space-time view can characterize the complicated deformation field in TBG concisely.

To set up the vierbein formalism, we need to choose an axis of rotation. As shown in Fig. 1 the rotation axis is at the middle plane $z = 0$ of TBG. We choose this as the origin. The two layers are located in $z = \pm \frac{h}{2}$ respectively. The rotation axis goes through the sites of A sublattice from each layer for untwisted AA stacking bilayer graphene. The sublattice notation for untwisted AA stacking bilayer graphene is indicated by Fig. 1. Then we consider the homogeneous twist (deformation) along the z axis. The interlayer distance is h . As elasticity theory, we define the deformation field \mathbf{u} at a given point as the oriented vector connecting the point before deformation and the counterpart after deformation. Thus the transformation of the deformation field under rotation is the following

$$\begin{pmatrix} u_x(\mathbf{r}) \\ u_y(\mathbf{r}) \end{pmatrix} = R \begin{pmatrix} u_x(R^{-1}\mathbf{r}) \\ u_y(R^{-1}\mathbf{r}) \end{pmatrix}, \quad R = \begin{pmatrix} \cos \phi & -\sin \phi \\ \sin \phi & \cos \phi \end{pmatrix}, \quad (1a)$$

$$R^{-1}\mathbf{r} = \begin{pmatrix} x \cos \phi + y \sin \phi \\ -x \sin \phi + y \cos \phi \end{pmatrix}. \quad (1b)$$

where ϕ is the twist angle. Note that, Eq. (1b) is just the transformation rule of a planar vector field. So after the deformation, the coordinates shift to $y^i(\mathbf{x})$, as shown in Fig. 2. The component of deformation vector is denoted by i . One can by definition get the vierbein and metric of the effective curved space. For simplicity, we choose the gauge for the vierbein and let it equal to the Jacobian transformation between the curved coordinate and flat counterpart [39–43]. So the curved space coordinate and vierbein can be expressed as follows

$$y^i(\mathbf{x}) = x^i + u^i(\mathbf{x}), \quad e_a^\mu = \frac{\partial y^\mu}{\partial x^a} = \delta_a^\mu + \partial_a u^\mu, \quad \xi_\mu^a = (e_a^\mu)^{-1}, \quad (2)$$

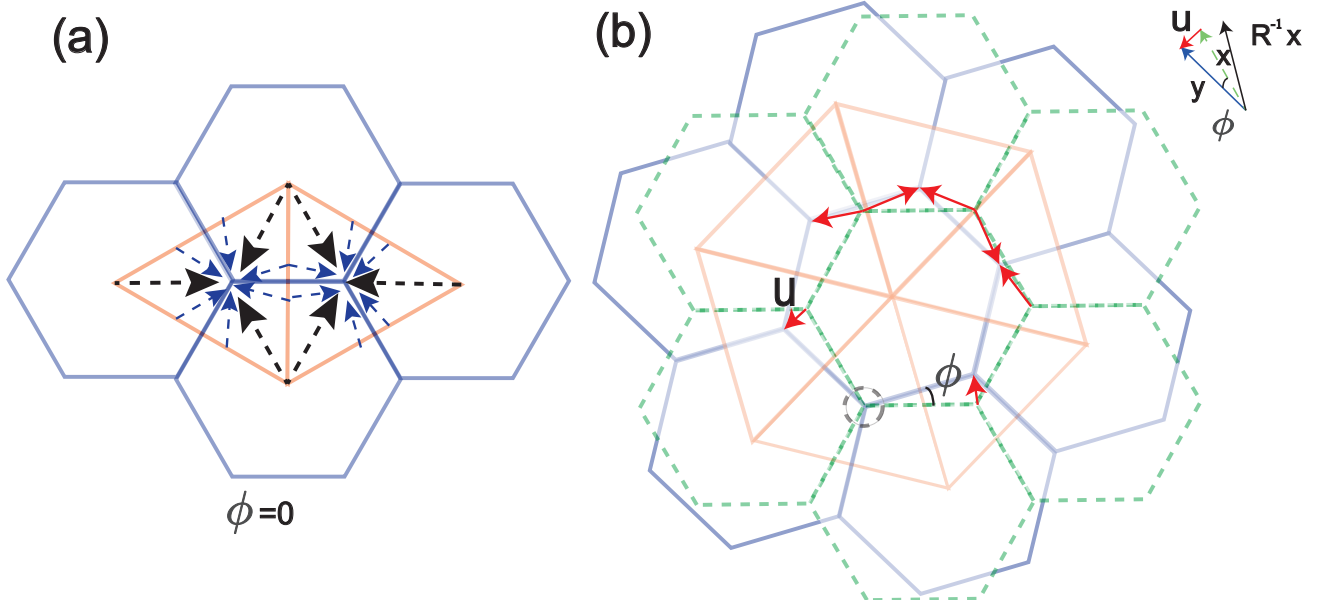


Figure 2. Bilayer configuration and twist geometries. (a) Untwisted bilayer graphene. The orange triangle is the deformation domain wall. The dashed arrows show the deformation vector field. (b) Twisted bilayer graphene with twist angle ϕ . The solid blue honeycomb lattice denotes the top layer (twisted one). The dashed green counterpart is the bottom layer (fixed one). The orange triangle corresponds to a twisted deformation domain wall. The deformation vector for a given site can be obtained by connecting the site in the untwisted lattice to the nearest center of the triangle domain wall in the twisted lattice. The minifigure in (b) shows the relation between vectors \mathbf{x} , \mathbf{u} , \mathbf{y} , and $R^{-1}\mathbf{x}$ at a given point.

The Greek symbols $\mu, \nu \dots = 0, 1, 2, 3$ denote components of the curved space-time coordinate, while the alphabets $a, b \dots = 0, 1, 2, 3$ denote the flat space-time counterpart or the internal indices of pseudo-spin. (0 denotes time component and 1,2,3 denotes x, y, z spatial components respectively.) Intuitively, we assume there is a tight binding picture and the lattice is a rigid structure. Although previous formulations have suggested that lattice relaxation helps to isolate the flat band from other higher bands [22, 26, 44, 45], for simplicity we do not consider lattice relaxation here. Note, since lattice relaxation can significantly modulate electron-phonon interaction and introduce strain in TBG, there may be non-vanishing torsion under our geometric theory. The layer may be corrugated and thus no longer form a plane. This can lead to added complexity. However, one can improve on this by introducing an out of plane deformation u_z [5] to capture the physics of corrugated TBG. Thus, we ignore lattice relaxation for simplicity.

To illustrate the deformation singularity [46] at domain walls of the twisted bilayer lattice, one can draw out the Wigner-Seitz cell (dual triangular mesh) of the honeycomb lattice. For the points on the untwisted triangular mesh, the deformation field will be multi-valued. Particularly, points on edges of domain walls have two values while points on vertices of domain walls have six values, see Fig. 2. Then one can write the deformation field for a given point by connecting it with the nearest center of the twisted triangular mesh in Fig. 2 to obtain

$$u_x(\mathbf{r}') = \left[\left(\frac{3}{2}(p+q) - x_1 \right) \vartheta \left(\frac{3}{2}(p+q) + \frac{1}{2} - x_1 \right) \right. \\ \vartheta \left((x_1 - \sqrt{3}x_2) - (3p-1) \right) \vartheta \left((x_1 + \sqrt{3}x_2) - (3q-1) \right) + \\ \left. \left(\frac{3}{2}(p+q) + 1 - x_1 \right) \vartheta \left(x_1 - \left(\frac{3}{2}(p+q) + \frac{1}{2} \right) \right) \right. \\ \vartheta \left((3p+2) - (x_1 - \sqrt{3}x_2) \right) \vartheta \left((3q+2) - (x_1 + \sqrt{3}x_2) \right) \left. \right] \\ \times \left(\frac{z}{h} + \frac{1}{2} \right) \vartheta \left(z + \frac{h}{2} \right) \vartheta \left(\frac{h}{2} - z \right). \quad (3a)$$

$$u_y(\mathbf{r}') = \left[\left(\frac{\sqrt{3}}{2}(q-p) - x_2 \right) \times \vartheta \left((x_1 - \sqrt{3}x_2) - (3p-1) \right) \right. \\ \vartheta \left((x_1 + \sqrt{3}x_2) - (3q-1) \right) \vartheta \left((3p+2) - (x_1 - \sqrt{3}x_2) \right) \\ \left. \vartheta \left((3q+2) - (x_1 + \sqrt{3}x_2) \right) \right] \left(\frac{z}{h} + \frac{1}{2} \right) \vartheta \left(z + \frac{h}{2} \right) \vartheta \left(\frac{h}{2} - z \right). \quad (3b)$$

$$p = \text{floor} \left(\frac{x_1 - \sqrt{3}x_2 + 1}{3} \right), \quad q = \text{floor} \left(\frac{x_1 + \sqrt{3}x_2 + 1}{3} \right), \\ x_1 = x \cos \phi + y \sin \phi, \quad x_2 = -x \sin \phi + y \cos \phi, \quad (3c)$$

where $\vartheta(x)$ is the Heaviside function which describes the location of the triangular mesh (domain walls of the deformation field) and $\text{floor}(x)$ means the least integer function. By

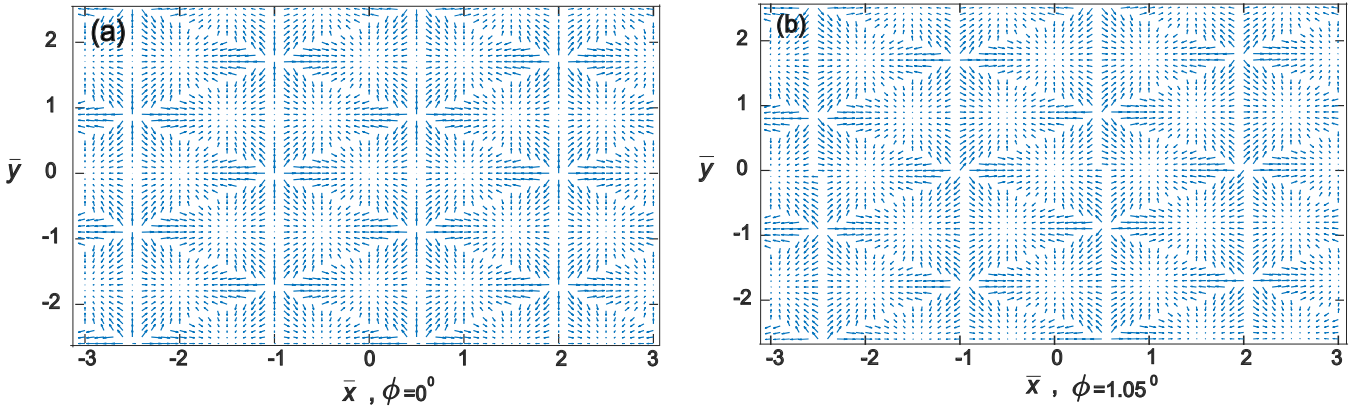


Figure 3. Plot of the deformation field in the whole plane for AA stacking bilayer graphene according to Eq. (3a), Eq. (3b), Eq. (3c) for magic angle ϕ . The arrows show the local deformation vector \mathbf{u} in Eq. (2). One can observe that the domain walls of deformation form a triangular mesh. Deformation field at (a) zero twisted angle and (b) the first magic angle given by Eq. (3a), Eq. (3b), Eq. (3c). Note, $\bar{x} = x/1.24 \text{ \AA}$, $\bar{y} = y/1.24 \text{ \AA}$ are the dimensionless length in units of lattice constant.

examination one can see that $(\partial_x \partial_y - \partial_y \partial_x)\mathbf{u} \neq 0$, which implies a non-vanishing spin connection in the effective curved space. The coordinates are related by $\mathbf{r}' = (x_1, x_2, z)^T = R^{-1} \mathbf{r}$ and $\mathbf{r} = (x, y, z)^T$. The deformation field $\mathbf{u}(\mathbf{r})$ in the laboratory frame can be obtained using Eq. (1b). As a check, we can set $\phi = 0$ in Eq. (3a) (3b) (3c). With this substitution one can recover the deformation field for the untwisted bilayer graphene. In Fig. 2(a), the deformation vectors in the two neighboring triangular cells have been drawn only.

A detailed distribution of the deformation field is presented in Fig. 3. The field for each site is shown by an arrow which connects the site in an untwisted lattice and the center of the nearest triangular domain wall with its twisted counterpart. For the untwisted site located on the triangular domain wall mesh, it will have a singular deformation. We observe that the deformation domain wall forms a triangular mesh in the whole plane. When crossing the domain wall, the deformation field component which is perpendicular to the domain wall changes direction while the component parallel to domain wall remains unchanged.

IV. DIRAC EQUATION WITH SPIN CONNECTION

In this section we elucidate how to get torsion free spin connection via vierbein and solve the relevant curved space Dirac equation with spin connection. One can first start from the flat metric under Cartesian coordinate.

$$ds^2 = \eta_{ab} dx^a dx^b = -dt^2 + dx^2 + dy^2 + dz^2, \quad (4)$$

where $\eta_{ab} = \text{diag}(-1, 1, 1, 1)$. Assuming there is no torsion since we are considering rotation but no dislocation for the relative displacement between two layers the spin connection can be expressed using the vierbein. This will introduce a compact gauge field which characterizes the minimal coupling between effective curved space-time and pseudospin, that is the SU(2) gauge field or pseudo magnetic vector potential [12, 22, 24]. This pseudo magnetic field can generate

the strongly correlated flat bands and fractional quantum Hall effect (FQHE). The torsion free spin connection (expressed by flat background embedded space-time coordinate) is expressed as follows [47]

$$\begin{aligned} (\omega_a)_{bc} = & \frac{1}{2} \eta_{bd} \xi_\mu^d (\partial_c \partial_a - \partial_a \partial_c) u^\mu + \frac{1}{2} \eta_{cd} \xi_\mu^d (\partial_a \partial_b - \partial_b \partial_a) u^\mu \\ & + \frac{1}{2} \eta_{ad} \xi_\mu^d (\partial_c \partial_b - \partial_b \partial_c) u^\mu + \frac{1}{2} (\partial_a \eta_{bc} + \partial_c \eta_{ba} - \partial_b \eta_{ca}). \end{aligned} \quad (5)$$

The vierbein and deformation field in Eq. (5) can be obtained from Eq. (2). If the reference metric for an untwisted space-time is a flat one (like Euclidean or Minkowskian in our case), the spin connection can be reduced to the following form

$$\begin{aligned} (\omega_a)_{bc} = & \frac{1}{2} \eta_{bd} \xi_\mu^d (\partial_c \partial_a - \partial_a \partial_c) u^\mu + \frac{1}{2} \eta_{cd} \xi_\mu^d (\partial_a \partial_b - \partial_b \partial_a) u^\mu \\ & + \frac{1}{2} \eta_{ad} \xi_\mu^d (\partial_c \partial_b - \partial_b \partial_c) u^\mu. \end{aligned} \quad (6)$$

However when the background metric is curved, for example, cylindrical coordinate metric, the last term in Eq. (5) will not vanish. One should also notice that only when the deformation field u^μ has a discontinuous second order mixed derivative, the deformation will produce a non-vanishing spin connection.

In principle, one can get the analytic form of the expression $(\partial_x \partial_y - \partial_y \partial_x)\mathbf{u}$ from Eq. (3a) – Eq. (3c) for obtaining spin connection in Eq. (6). However, obtaining the complete form of $(\partial_x \partial_y - \partial_y \partial_x)\mathbf{u}$ analytically is complicated, so in practice one should determine the expression numerically. The general term in $(\partial_x \partial_y - \partial_y \partial_x)\mathbf{u}$ is the product of the Dirac delta function, Heaviside function, Floor function, and the derivative of the floor function, that is, $(\partial_x \partial_y - \partial_y \partial_x)\mathbf{u} \approx \sum_{(1,2,3)} \mathbf{A}_{123} \delta(\text{edge}_1) \text{floor}'(\text{edge}_1) \theta(\text{edge}_2) \theta(\text{edge}_3)$. To avoid numerical singularity we introduce a Lorentzian width Γ for the domain wall in the spin connection [Eq. (6)] and the vierbein [Eq. (2)], instead of using the Dirac delta function. Γ is a

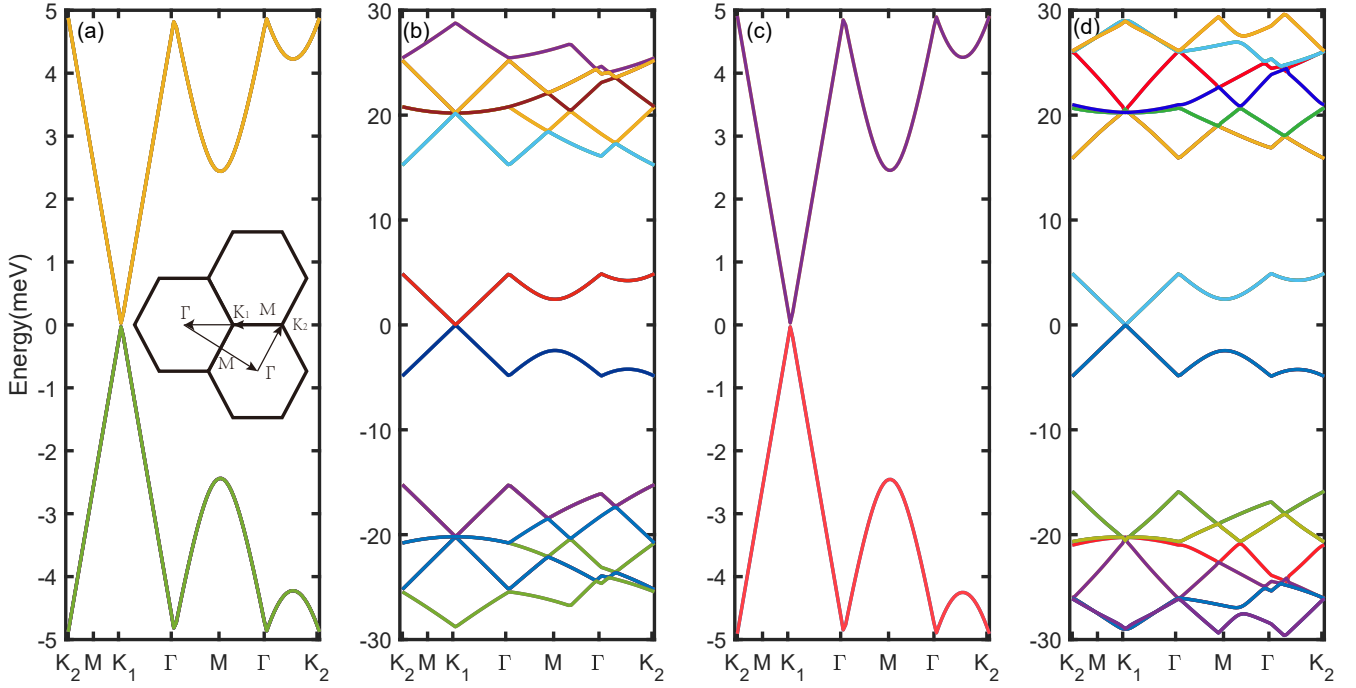


Figure 4. Flat band at magic angle ($\phi = 1.05^\circ$) based on Dirac equation [Eq. (9b)]. Bands closest to the Fermi surface ($\epsilon = 0$) have been plotted. With $\Gamma = 10^{-5}$ (a) Two-fold degenerate energy bands (four in total) and (b) Twenty-four bands. With $\Gamma = 10^{-3}$ (c) Four bands and (d) 28 bands with size $L_x = 15, L_y = 15$. The mesh density is $N_x = N_y = 15$. The band width is about 5 meV. In subsequent figures, we show several bands around the Fermi energy unless otherwise specified. That is we assume the system is always at half filling. The origin of the \mathbf{k} space is one of the moiré Dirac points, K_1 .

small value with dimension of length, which implies broadening of the deformation due to some disorder, phonon or fluctuation (within a phenomenological analysis, this would be a tunable parameter). More details can be found in Eq. (A3) from Appendix A.

We can obtain the total non-abelian connection by contracting its components with the pseudo spin-generators

$$\begin{aligned} \omega_\mu &= \frac{i}{2}(\omega_\mu)_{ab}\Sigma^{ab}, \quad \Sigma^{ab} = \frac{i}{4}[\gamma^a, \gamma^b], \quad \omega_a = e_a^\mu \omega_\mu, \\ \gamma^0 &= \begin{pmatrix} 0 & I \\ I & 0 \end{pmatrix}, \quad \gamma^i = \begin{pmatrix} 0 & \sigma^i \\ -\sigma^i & 0 \end{pmatrix}, \quad i = 1, 2, 3, \end{aligned} \quad (7)$$

where $[\gamma^a, \gamma^b] = \gamma^a\gamma^b - \gamma^b\gamma^a$. The spin connection will modulate the hopping (for the tight binding model) and the covariant derivative (for the continuum model) as

$$t_{ij} \rightarrow t_{ij} \exp\left(\frac{i}{4}dx_{ij}^a \left[(\omega_a(r_i))_{bc} + (\omega_a(r_j))_{bc}\right] \Sigma^{bc}\right), \quad (8a)$$

$$\partial_a \rightarrow D_a = \partial_a + \omega_a. \quad (8b)$$

For the first expression in Eq. (8b), the model corresponds to a non-abelian Hofstadter model with inhomogeneous flux [23,

48–50]. Here, since we are considering a continuous Dirac effective model, an alternate way to introduce spin connection in Eq. (8b) will be implemented.

We consider a curved space Dirac action for TBG which has been studied in strained graphene system [51] and the Kitaev honeycomb lattice model with Kekulé distortion [52]. Thus we consider an effective theory at charge neutrality (half filling). The spin- $\frac{1}{2}$ quantum field in Riemannian space-time is governed by the following action and the Hamiltonian density (for TBG, for single valley approximation) [52–54]

$$S = i \int d^{3+1}x |\xi| (\bar{\psi} \gamma^\mu D_\mu \psi + im \bar{\psi} \psi), \quad (9a)$$

$$H = -i|\xi| [v_f (\bar{\psi} \gamma^j \partial_j \psi + \bar{\psi} \gamma^j \omega_j \psi) + im \bar{\psi} \psi], \quad (9b)$$

$$g_{\mu\nu} = \frac{\partial x^a}{\partial y^\mu} \eta_{ab} \frac{\partial x^b}{\partial y^\nu} = \xi_\mu^a \eta_{ab} \xi_\nu^b, \quad (9c)$$

where $|\xi| = |\det(\xi_\mu^a)| = \sqrt{|\det(g_{\mu\nu})|}$, $D_\mu\psi = \partial_\mu\psi + \omega_\mu\psi$, $\mu = 0, 1, 2, 3$, $j = 1, 2, 3$. The spin connection in Eq. (9b) will be given by Eq. (7). By introducing $\psi_{\mathbf{k}}(\mathbf{r}) = \exp(i\mathbf{k} \cdot \mathbf{r})u_{\mathbf{k}}(\mathbf{r})$ and diagonalizing the Hamiltonian one can get the bands for arbitrary twisted angle. Even though \mathbf{k} is not a good quantum number in this case, one has to choose a \mathbf{k} in the background Euclidean space. The Dirac equation in the moiré scale (with about 1000 atoms per supercell) is computed using twisted boundary condition [55–57].

$$\psi_{\mathbf{k}}(x + L_x, y) = \exp\left(-\int_x^{x+L_x} ds \omega_x\right)\psi_{\mathbf{k}}(x, y), \quad (10a)$$

$$\psi_{\mathbf{k}}(x, y + L_y) = \exp\left(-\int_y^{y+L_y} ds \omega_y\right)\psi_{\mathbf{k}}(x, y). \quad (10b)$$

We present a numerical solution [58] for the (non-Hermitian) Dirac equation in effective curved space (in a finite size $x \in [0, L_x]$, $y \in [0, L_y]$, with the rotation axis located at (0,0)). All length scales will be in units of $a_0 = 1.42 \text{ \AA}$, the intralayer nearest distance between carbon atoms unless specified otherwise, at the first magic angle $\theta \approx 1.05^\circ$ as shown in Fig. 4. The discretization is implemented in the background Euclidean space with relevant spin connection and metric. The moiré BZ notation is given by the bare Fermi velocity $v_f = 10^6 \text{ m/s}$, interlayer distance $h = 0.5 \times 1.42 = 0.71 \text{ \AA}$ and the bare reduced interlayer interaction $w = 0.11 \text{ eV}$ (acting as an effective mass) as in Ref. 1. The result of the lowest band width in Fig. 4 is near the flat band width given by the BM model or DMRG (about 5meV) [33, 59]. So this geometric theory can reproduce the flat bands given by former theory like [13] qualitatively. Only the real part of bands has been shown.

In a curved background, the Hamiltonian [Eq. (9b)] will generally be non-Hermitian, as explained in detail in Appendix A. Though the bands are usually complex, one can numerically verify that eigenvalues $a + ib, a - ib, -a + ib, -a - ib$ will appear simultaneously as shown in Fig. 6. Very recently, Refs. [60–62] have argued the duality between non-Hermitian model in flat space and Hermitian system in curved space. So treating a non-Hermitian Dirac action is justified. In fact, one can always construct a Hermitian Hamiltonian by substituting $S \rightarrow \frac{1}{2}(S + S^\dagger), H \rightarrow \frac{1}{2}(H + H^\dagger)$ as in Ref. [63]. However, in order to ensure the existence of nearly zero energy bands, one should introduce the covariant derivation operator $-iD_\mu$ in the action and not $\frac{1}{2}(-iD_\mu + i\bar{D}_\mu)$. The existence of zero energy band in the deformed bilayer graphene is ensured by the Atiyah-Singer index theorem [64]. This is why in this article we focus on the non-Hermitian Dirac Hamiltonian.

In Fig. 5, we observe that there are no energy bands around the Fermi surface for the Hermitian Hamiltonian. The lowest bands are no longer as flat as its non-Hermitian counterpart. Since the magnitude of bandwidth in Fig. 5(a) and 5(b) is at least 0.1 eV, if one decreases the domain wall width to $\Gamma = 10^{-5}$ (in the unit of a_0) as in Fig. 5(c) and 5(d), the energy scale of the lowest bands will increase about an order of mag-

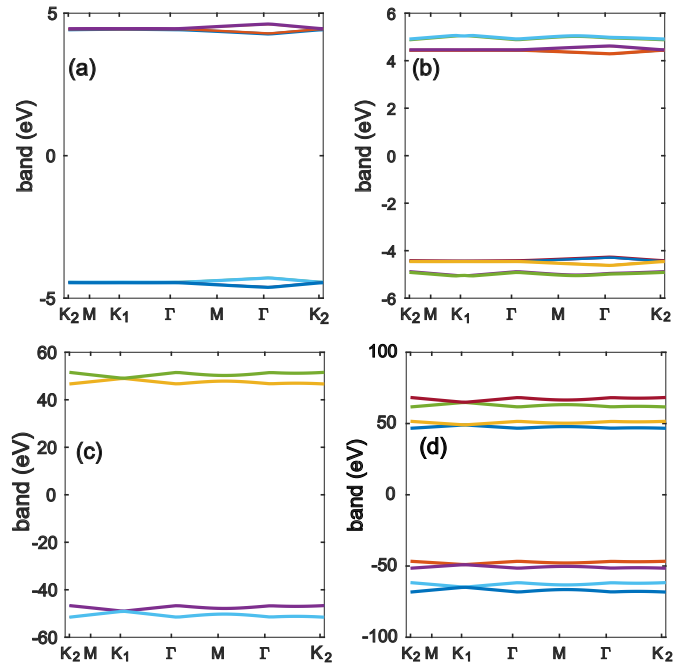


Figure 5. For Hermitian model, we show the result for 8 and 12 bands near $\epsilon = 0$ with $\Gamma = 10^{-3}$, $L_x = L_y = 7$ in panels (a) and (b), respectively. In panels (c) and (d), we show the counterpart for parameter $\Gamma = 10^{-5}$, $L_x = L_y = 7$. Mesh density $N_x = N_y = 7$. Panel (c) shows 4 bands and Fig (d) shows 8 bands near $\epsilon = 0$ respectively.

nitude. Whereas in Fig. 4, the domain wall width will not significantly influence the lowest band structure. The crucial flat bands still survive. Besides, there is an alternative way to argue that the TBG Hamiltonian should be non-Hermitian. One can design an adiabatic process for twisting the bilayer from AA stacking to one of the magic angles. If the TBG Hamiltonian is Hermitian for all twisted angle, the wave function for AA stacking and magic angle can be connected by a local unitary transformation (adiabatic time evolution). However, AA stacking bilayer graphene is topologically trivial while MATBG hosts stable topological phase [6]. So during the adiabatic twisting process, there must be a topological phase transition. Thus, the assumption for adiabatic unitary evolution is incorrect [65, 66]. (For realistic situation with hBN substrate, one can expect there is always gap between ground state and excited state for initial and final wave function.) There should be at least one instant of non-Hermitian Hamiltonian during the adiabatic twisting process. One can observe that for the lowest energy levels in Fig. 6, the imaginary part has the same magnitude as the real part. So the non Hermiticity will not cause apparent broadening for the lowest band's density of state. Such spectrum is protected by so-called bi-chiral symmetry in certain parameter regime [49]. The discontinuity of $\frac{\partial E_{\mathbf{k}}}{\partial k}$ at Γ, \mathbf{K}_2 in Fig. 4 can be interpreted as the anisotropy of the Fermi velocity at Γ, \mathbf{K}_2 [67] in moiré BZ since at these \mathbf{k} points the \mathbf{k} path changes direction.

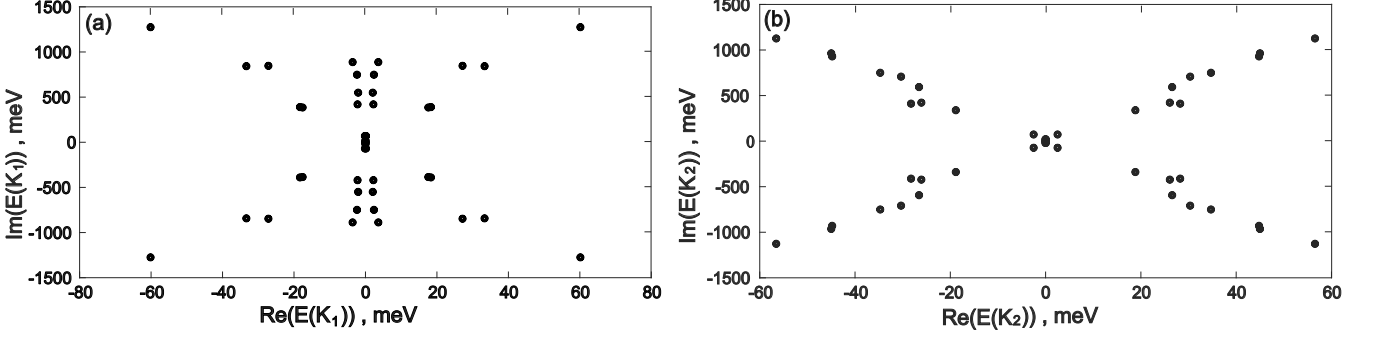


Figure 6. Real and imaginary values of the energy. (a) Illustrates the complex energy with $\Gamma = 10^{-3}$, $L_x = L_y = 7$ at \mathbf{K}_1 . (b) shows the complex energy with $\Gamma = 10^{-3}$, $L_x = L_y = 7$ at \mathbf{K}_2 . Mesh density $N_x = N_y = 7$. The spectra are symmetric about the real and imaginary axis.

V. THEORY FOR ROTATING BILAYER GRAPHENE (RBG)

In this section we generalize our geometric theory from TBG to RBG. This is the relative rotating bilayer graphene configuration with constant angular velocity ω_0 . The motivation to investigate RBG is that under the vierbein formalism, a RBG will generate a spin connection with non-vanishing time component ω_t , which can mix with the usual AA phase (generated by periodic evolution) [68]. As a result new topological phase or phases will arise as evidenced from the non-trivial Bott index regime in Fig. 8. Another motivation is that although Floquet engineering of TBG has been systematically studied [18, 19, 69, 70], most of them have focused on light frequency driven regime or sliding TBG as a 2d Thouless pump [20, 71]. The non-adiabatic structurally rotating driving TBG is still in need of investigation [72]. The non-adiabatic Thouless pump has only been reported in waveguide array [73]. Actually, the vierbein formalism can be naturally generalized to RBG. The only difference is that one should use a four dimensional metric and let $\phi = \omega_0 t$. The Hamiltonian for time-dependent curved space-time Dirac fermion is written as [58]

$$H = -i|\xi|[-\bar{\psi}\gamma^0\omega_t\psi + v_f(\bar{\psi}\gamma^j\partial_j\psi + \bar{\psi}\gamma^j\omega_j\psi) + im\bar{\psi}\psi]. \quad (11)$$

When the bilayer graphene starts rotating, another factor which will cause non hermiticity is the boost generator $\Sigma^{0j} = \frac{i}{4}[\gamma^0, \gamma^j]$, ($j = 1 \dots 3$) in Eq. (7). It is an anti-Hermitian operator under dynamic vierbein situation in RBG. As a result, the gauge transformation factor in (dynamic) twisted boundary condition [Eq. (10a), Eq. (10b)] will be a non-unitary one, which can be traced back to the non-compact nature of the Poincaré group [74]. So the system turns out to be a non-Hermitian Floquet system. One should also be cautious that for a general twist angle there is no moiré BZ. Since for a general incommensurate twisted angle, there is no strict translation symmetry our vierbein formalism in the \mathbf{k} space will also be a curved one for general incommensurate twisted angle [6, 75]. So in the following calculations, we will manipulate in real space instead of \mathbf{k} space.

To capture the quasiperiodic or incommensurate nature of RBG, we consider Bott index to relate the charge pumping during rotation driving [76–82].

$$\begin{aligned} P(t) &= \sum_{\text{Re}(E_n(t)) < \mu} |\psi_n(t)\rangle\langle\tilde{\psi}_n(t)|, \\ U_x &= I - P + P \exp\left(i2\pi\frac{x}{L_x}\right)P, \\ U_y &= I - P + P \exp\left(i2\pi\frac{y}{L_y}\right)P, \end{aligned} \quad (12a)$$

$$\begin{aligned} I_{Bott}^x(t) &= \frac{1}{2\pi} \int_0^t \text{Im}[\text{Tr}(\ln(U_x(t' + dt')U_{-x}(t')))] \\ &= \frac{1}{2\pi} \int_0^t dt' \partial_{t'} [\text{Im}(\ln(\det(U_x(t'))))], \end{aligned} \quad (12b)$$

$$\begin{aligned} I_{Bott}^y(t) &= \frac{1}{2\pi} \int_0^t \text{Im}[\text{Tr}(\ln(U_y(t' + dt')U_{-y}(t')))] \\ &= \frac{1}{2\pi} \int_0^t dt' \partial_{t'} [\text{Im}(\ln(\det(U_y(t'))))], \end{aligned} \quad (12c)$$

$$I_{Bott} = I_{Bott}^x + I_{Bott}^y. \quad (12d)$$

Let V be the eigenstate matrix of the Hamiltonian. Each column corresponds to the eigenstate $\{|\psi_n\rangle\}$, while $\{|\tilde{\psi}_n\rangle\}$ in Eq. (12a) is the counterpart for matrix $(V^{-1})^\dagger$ (biorthogonal basis [83, 84]). $I_{Bott}(T)$ can be considered as the charge pumping per period for a given finite size $L_x \times L_y$ rectangle region [71, 76]. The factor $U_x(t' + dt')U_{-x}(t')$ contains the effect of the AA phase since it relates the gauge connection defining on the bundle whose base manifold is a 1d periodic time parameter in S^1 .

The result of the RBG Bott index is shown in Fig. 7 which shows the total contribution along with the individual contributions in the x and the y direction. The figure suggests that the Bott index can transition between trivial to non-trivial

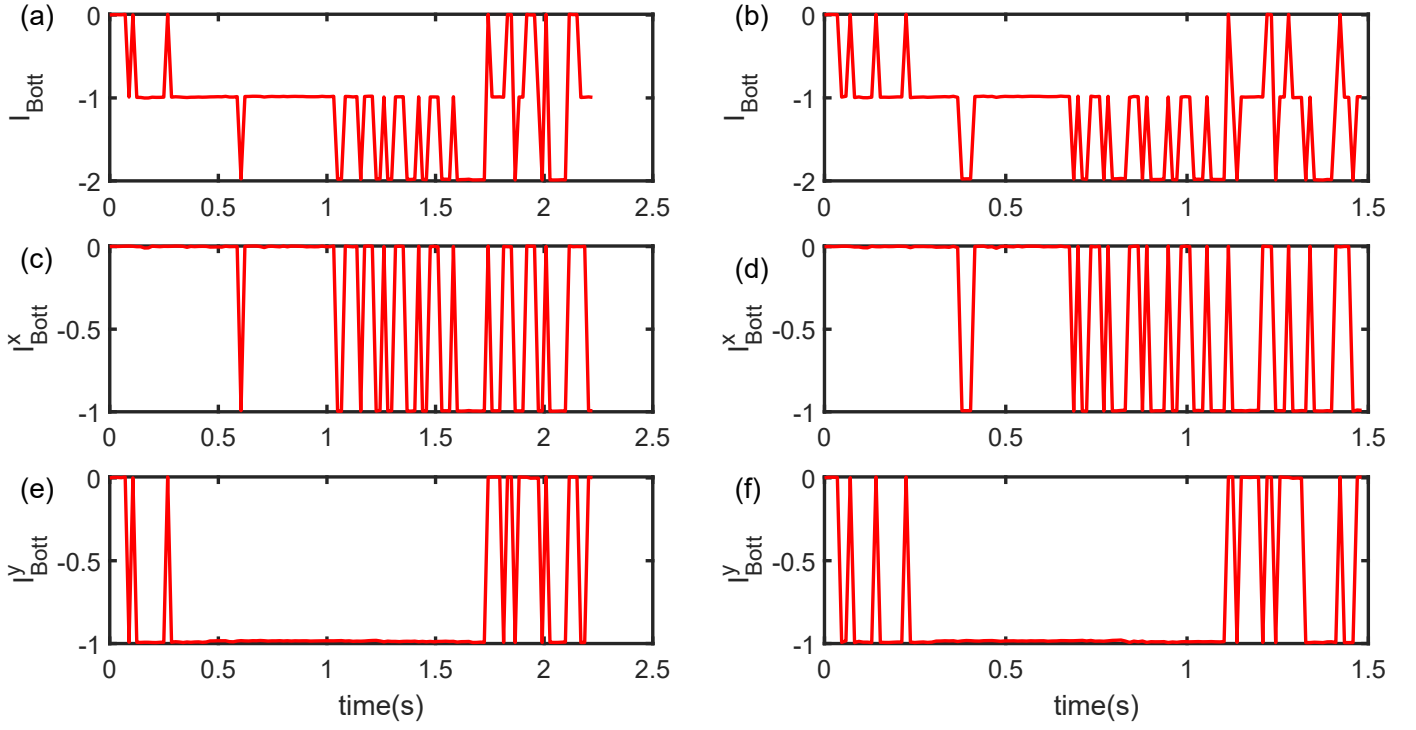


Figure 7. Bott index in one period when $\Gamma = 0.5$ with size $L_x = 15, L_y = 15\sqrt{3}$. The thickness of monolayer graphene is $h = 2.36$. The mesh density $N_x = N_y = 15$. Panels (a), (c), and (e) are the total Bott index, Bott index in the x direction, and the y direction [Eq. (12d), Eq. (12b), Eq. (12c)] under 0.943 rad/s of driving frequency, respectively. While (b), (d), and (f) are for 1.414 rad/s of driven frequency. For each diagram, the number of the time slices is 125, that is, the time step is $T/125$.

topological sectors. We observe from the figures that the Bott index variation is similar over the time cycle displayed. This variation guides us to the instantaneous time dependence of the Bott index. Thus, to obtain information on any potential topological transition, we have to study the behavior of this index across various frequency cycles.

In Fig. 8, we give out the dependence of Bott index $I(\omega_0, T)$ on driven frequency ω_0 . We can see that in certain driven frequency regime, the finite size $L_x = 15, L_y = 15\sqrt{3}$ RBG system will hold non-trivial Bott index. Note that here we still use Cartesian coordinate instead of the hexagonal coordinate used in [85]. So the structural rotation periodic driving may cause new topological phase. During the simulation, one assumes that the RBG system stays in half filling all the time. As bilayer graphene starts rotating and achieves steady state it will act as a non-adiabatic Thouless pump [73]. In one period, the charge pumping will be quantized and can be recorded by an ammeter. Numerical result shows that the quantized charge pumping will generally depend on the size and the driving frequency. To show the relation between Bott index and pumping charge consider the expectation of a wave packet center which

can be expressed as [76].

$$\begin{aligned} \langle x(t) \rangle &= \langle \psi(t) | \hat{x} | \psi(t) \rangle = \frac{L_x}{2\pi} \text{Arg}(U_x(t)), \\ \langle y(t) \rangle &= \langle \psi(t) | \hat{y} | \psi(t) \rangle = \frac{L_y}{2\pi} \text{Arg}(U_y(t)). \end{aligned} \quad (13)$$

In the above we used the abbreviation $\text{Arg} = \text{ImTrln}$. The corresponding polarized current pumping in an infinitesimal time interval can be related to the Bott index as

$$\begin{aligned} j_x(t)\Delta t &= \text{Arg}(U_x(t + \Delta t)U_{-x}(t)), \\ j_y(t)\Delta t &= \text{Arg}(U_y(t + \Delta t)U_{-y}(t)), \\ I_{Bott}^x(T) &= \int_0^T dt j_x(t), \quad I_{Bott}^y(T) = \int_0^T dt j_y(t). \end{aligned} \quad (14)$$

Thus the Bott index is directly connected to real space polarized pump current which can be measured directly. When the RBG achieves a stable state we have the following relationship amongst the current. $\partial_t Q + I_x + I_y + I_z = 0$, $\partial_t Q = 0$, $I_x + I_y = I_{Bott} = -I_z = -I_{\text{measure}}$. So the total pumping current (Bott index) can be measured by a vertical current.

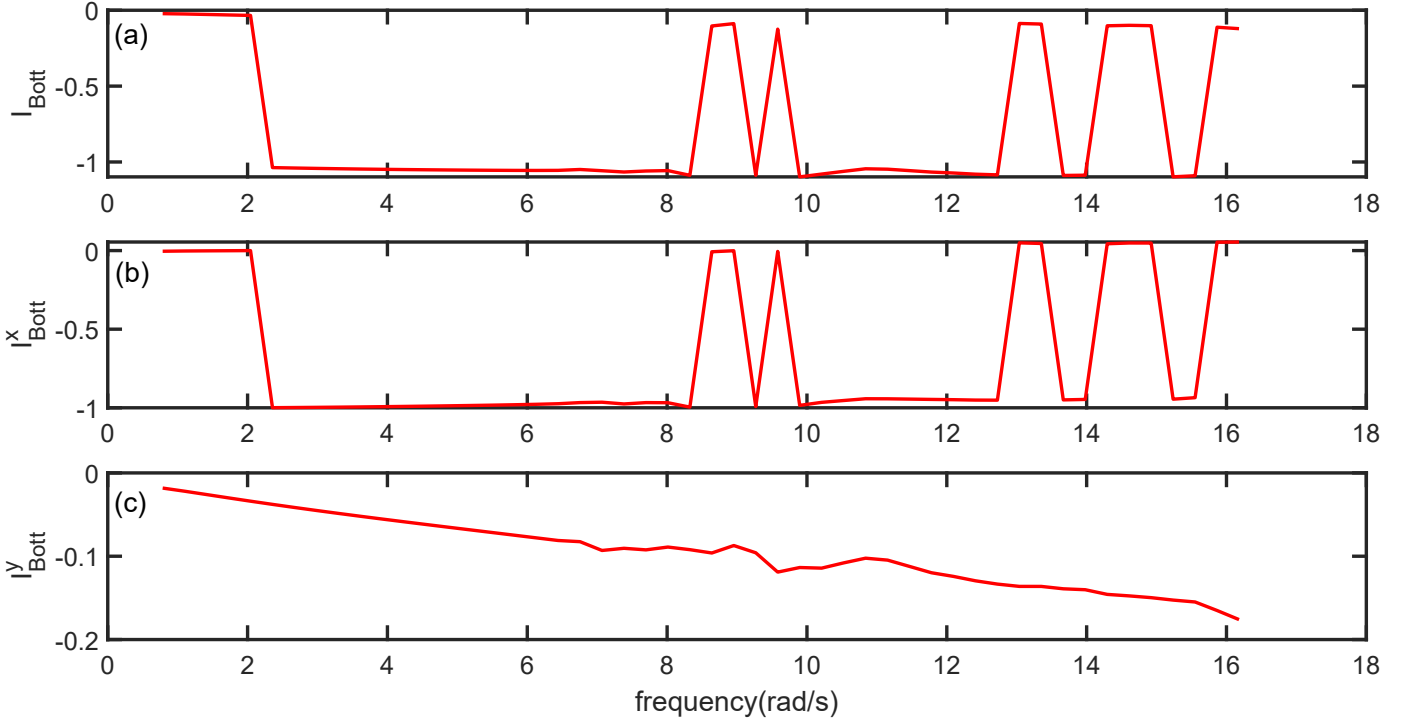


Figure 8. Bott index-driving frequency relation $I(\omega, T)$ when $\Gamma = 0.5$ with size $L_x = 15, L_y = 15\sqrt{3}, h = 2.36$. The mesh density is $N_x = N_y = 15$. Fig. (a), (b), (c) are I_{Bott} , I_{Bott}^x , I_{Bott}^y respectively. The frequency step in simulation is 0.314rad/s . The Bott indices for 50 different driven frequency are shown.

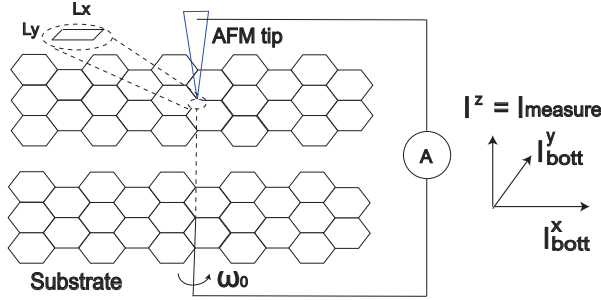


Figure 9. A simple scheme for realizing the measurement of RBG pumping current. In practice, rotating the substrate is more convenient. The total transverse pumping current can be measured by the vertical ammeter when the system achieves a stable state. The AFM tip is tailored according to the given finite size $L_x \times L_y$ rectangle.

VI. DISCUSSION AND CONCLUSION

We have developed a geometric effective theory for TBG with generic twist angle, which in principle can be generalized to other twisted bilayer Bravais lattice as long as the dual lattice is known and the atoms are homogeneous. For TBG,

by connecting a given point (the point we want to get its deformation field) and the nearest twisted triangle center we can get the deformation field for arbitrary twist angle and arbitrary position. This deformation can induce an effective SU(2) gauge field and curved space. The novel properties of the TBG can be interpreted as a geometric response. The numerical result of energy bands near the first magic angle for non-Hermitian Dirac Hamiltonian reproduces the flat bands. The discontinuity of $\partial E_{\mathbf{k}} / \partial k$ indicates the Fermi velocity anisotropy at high symmetry \mathbf{k} -points Γ and \mathbf{K}_2 . In addition, such effective geometric theory is applicable to the system with a dynamic vierbein such as in a RBG. For a rotating bilayer graphene with constant angular velocity ω_0 , the quantized pumping charge is illustrated by the Bott index which may be examined by transport experiment. A simple experimental proposal is also discussed to test the validity of the proposed Bott index theory for RBG. The topological property of RBG is controlled by the mixture of spin connection and the AA phase. Furthermore, note that the effective theory proposed in this article is still a single body theory, which does not take into account many body interaction. Thus, an explanation of the correlated insulating phase and the superconducting phase is beyond the scope of the present TBG and RBG formalism. Finally we suggest an experimental setup shown in Fig. 9 which can test

the validity of our proposed theoretical formulation. In this setup we consider the bilayer system being probed by an AFM tip which is tailored according to the given finite size of the system. With one of the layers fixed (say the upper one), the bottom is rotated, this should generate the transverse currents which can be measured within a transport setup.

ACKNOWLEDGMENTS

We thank Zhong-Bo Yan, Peng Ye, Jian-Peng Liu, Yi-Wen Pan, Jie Ren, Shi-Dong Liang, Jiannis K. Pachos, Matthew Horner, Jia-Qi Cai, Zi-Ang Hu, Ze-Min Huang, Hong Wu, Guang-Jie Li, Yu-Han Liu, Zhi-Qiang Zhang, Zi-Jian Xiong, Jian-Keng Yuan, Ge-Wei Chen, Ding-Kun Lian, Jun Li, Yun-Feng Chen for valuable discussion. J. Z. M. and D. X. Y. are supported by NKRDP-2017YFA0206203, NKRDP-2018YFA0306001, NSFC-11974432, GBABRF-2019A1515011337, and Leading Talent Program of Guangdong Special Projects. T. D. acknowledges funding support from Sun Yat-Sen University Grants No. OEMT-2019-KF-04 and No. OEMT-2017-KF-06.

Appendix A: Numerical implementation and non-hermiticity

The discretization of the ordinary partial (momentum) operator in curved space-time is given by

$$\begin{aligned} -i|\xi|\partial_x(j) &\rightarrow -i|\xi_j|\left[\frac{\delta_{j,j+1} - \delta_{j,j-1}}{2\Delta x}\right], \\ -i|\xi|\partial_x(j+1) &\rightarrow -i|\xi_{j+1}|\left[\frac{\delta_{j+1,j+2} - \delta_{j+1,j}}{2\Delta x}\right], \end{aligned} \quad (\text{A1})$$

where δ is the Kronecker symbol and j labels mesh site. Δx means the differential step. Apparently, if the vierbein has space-time dependence, i.e. $|\xi_j| \neq |\xi_{j+1}|$ generally, $-i|\xi|\partial_x$ will be a non-Hermitian operator, i.e. $-i|\xi_j|\frac{\delta_{j,j+1}}{2\Delta x} \neq \left(i|\xi_{j+1}|\frac{\delta_{j+1,j}}{2\Delta x}\right)^\dagger$. If one imposes the hermiticity, one should substitute $-i|\xi|\partial_x\psi \rightarrow -i|\xi|\left(\frac{1}{\sqrt{|\xi|}}\partial_x[\sqrt{|\xi|}\psi]\right)$ [86] or choose the Hermitian Hamiltonian. The discretization according to the former strategy takes

the form

$$\begin{aligned} -i|\xi|\left(\frac{1}{\sqrt{|\xi|}}\partial_x[\sqrt{|\xi|}(j)]\right) &\rightarrow \\ -i\left[\frac{\sqrt{|\xi_{j+1}|}|\xi_j|\delta_{j,j+1} - \sqrt{|\xi_j|}|\xi_{j-1}|\delta_{j,j-1}}{2\Delta x}\right], \\ -i|\xi|\left(\frac{1}{\sqrt{|\xi|}}\partial_x[\sqrt{|\xi|}(j+1)]\right) &\rightarrow \\ -i\left[\frac{\sqrt{|\xi_{j+2}|}|\xi_{j+1}|\delta_{j+1,j+2} - \sqrt{|\xi_{j+1}|}|\xi_j|\delta_{j+1,j}}{2\Delta x}\right]. \end{aligned} \quad (\text{A2})$$

Here the non-Hermitian discretization has been implemented to reproduce flat bands. Physically, momentum operators in curved space or incommensurate system are generally non-Hermitian. As an example, we consider one dimension $-i\int_{-\infty}^{+\infty} dx\psi^\dagger\partial_x\psi = -i(\psi^\dagger\psi|_{-\infty}^{+\infty} - \int_{-\infty}^{+\infty} dx(\partial_x\psi^\dagger)\psi)$. When $\psi^\dagger\psi|_{-\infty}^{+\infty} \neq 0$, momentum operators will be non-Hermitian. To do the numerical calculation, one should substitute the following functions in non-singular form when evaluating the vierbein [Eq. (2)], spin connection [Eq. (6)], and metric [Eq. (9c)].

$$\begin{aligned} \delta(x) &\approx \frac{1}{\pi} \frac{1}{x^2 + \Gamma^2}, \quad \vartheta(x) \approx \frac{1}{\pi} \arctan\left(\frac{x}{\Gamma}\right) + \frac{1}{2}, \\ \text{floor}'(x) = \sum_{k=-\infty}^{\infty} \delta(x-k) &\approx \sum_{k=-N}^N \frac{1}{\pi} \frac{1}{(x-k)^2 + \Gamma^2}, \end{aligned} \quad (\text{A3})$$

where Γ is a small value with the dimension of length, representing the broadening of the deformation domain wall due to some disorder, phonon or fluctuation. Here N is a large enough integer determined by twisted angle and size.

Appendix B: Second order derivative of rotating bilayer graphene

For RBG, one should consider more components of spin connection. However one should be cautious that the partial operator for twisted angle is not independent of the spatial partial operator. One has the following expressions

$$\begin{aligned} \phi &= \omega_0 t, \partial_t = \omega_0 \partial_\phi, \\ \partial_\phi &= x\partial_y - y\partial_x = x_2\partial_{x_1} - x_1\partial_{x_2}, \\ x_1 &= x \cos \phi + y \sin \phi, \quad x_2 = -x \sin \phi + y \cos \phi. \end{aligned} \quad (\text{B1})$$

Our target is to get the dynamic spin connection [Eq. (6)] in Eq. (11). In the basis of x_1, x_2 , we obtain

$$\begin{aligned}
(\partial_\phi \partial_x - \partial_x \partial_\phi) \begin{pmatrix} u^x \\ u^y \end{pmatrix} &= \left[-A_\phi C_\phi (\partial_{x_1} \partial_{x_2} - \partial_{x_2} \partial_{x_1}) - \frac{1}{2} E_\phi \partial_{x_1} - \frac{1}{2} D_\phi \partial_{x_2} \right] \begin{pmatrix} u'^x \\ u'^y \end{pmatrix}, \\
(\partial_\phi \partial_y - \partial_y \partial_\phi) \begin{pmatrix} u^x \\ u^y \end{pmatrix} &= \left[-B_\phi C_\phi (\partial_{x_1} \partial_{x_2} - \partial_{x_2} \partial_{x_1}) + \frac{1}{2} D_\phi \partial_{x_1} - \frac{1}{2} E_\phi \partial_{x_2} \right] \begin{pmatrix} u'^x \\ u'^y \end{pmatrix}, \\
(\partial_\phi \partial_z - \partial_z \partial_\phi) \begin{pmatrix} u^x \\ u^y \end{pmatrix} &= \left(A_\phi \left[-\frac{1}{2} E_\phi (\partial_z \partial_{x_1} - \partial_{x_1} \partial_z) + \frac{1}{2} D_\phi (\partial_{x_2} \partial_z - \partial_z \partial_{x_2}) \right] + B_\phi \left[\frac{1}{2} D_\phi (\partial_z \partial_{x_1} - \partial_{x_1} \partial_z) + \frac{1}{2} E_\phi (\partial_{x_2} \partial_z - \partial_z \partial_{x_2}) \right] \right) \begin{pmatrix} u'^x \\ u'^y \end{pmatrix}, \tag{B2}
\end{aligned}$$

where

$$\begin{aligned}
A_\phi &= x_1 \cos \phi - x_2 \sin \phi, & B_\phi &= x_1 \sin \phi + x_2 \cos \phi, \\
C_\phi &= \begin{pmatrix} \cos \phi & -\sin \phi \\ \sin \phi & \cos \phi \end{pmatrix}, & D_\phi &= \begin{pmatrix} 1 + \cos 2\phi & -\sin 2\phi \\ \sin 2\phi & 1 + \cos 2\phi \end{pmatrix}, \\
E_\phi &= \begin{pmatrix} \sin 2\phi & -(1 - \cos 2\phi) \\ 1 - \cos 2\phi & \sin 2\phi \end{pmatrix}. \tag{B3}
\end{aligned}$$

Here the abbreviations are $u^x = u^x(\mathbf{r})$, $u'^x = u^x(R^{-1}\mathbf{r})$, and so as u'^y . Subsequently, one can get the analytic form of $(\partial_{x_1} \partial_{x_2} - \partial_{x_2} \partial_{x_1})u'^x$, and so as u'^y .

[1] R. Bistritzer and A. H. MacDonald, PNAS **108**, 12233 (2011).
[2] Y. Cao, V. Fatemi, A. Demir, S. Fang, S. L. Tomarken, J. Y. Luo, J. D. Sanchez-Yamagishi, K. Watanabe, T. Taniguchi, E. Kaxiras, R. C. Ashoori, and P. Jarillo-Herrero, Nature **556**, 80 (2018).
[3] Y. Cao, V. Fatemi, S. Fang, K. Watanabe, T. Taniguchi, E. Kaxiras, and P. Jarillo-Herrero, Nature **556**, 43 (2018).
[4] J. Liu, Z. Ma, J. Gao, and X. Dai, Phys. Rev. X **9**, 031021 (2019).
[5] J. Liu and X. Dai, Phys. Rev. B **103**, 035427 (2021).
[6] Z. Song, Z. Wang, W. Shi, G. Li, C. Fang, and B. A. Bernevig, Phys. Rev. Lett. **123**, 036401 (2019).
[7] H. C. Po, L. Zou, T. Senthil, and A. Vishwanath, Phys. Rev. B **99**, 195455 (2019).
[8] M. J. Park, Y. Kim, G. Y. Cho, and S. Lee, Phys. Rev. Lett. **123**, 216803 (2019).
[9] A. Chew, Y. Wang, B. A. Bernevig, and Z.-D. Song, arXiv:2108.05373.
[10] D. Rodan-Legrain, Y. Cao, J. M. Park, S. C. de la Barrera, M. T. Randeria, K. Watanabe, T. Taniguchi, and P. Jarillo-Herrero, Nat Nanotechnol 10.1038/s41565-021-00894-4 (2021).
[11] A. Thomson, I. Sorensen, S. Nadj-Perge, and J. Alicea, arXiv:2105.02891.
[12] P. San-Jose, J. González, and F. Guinea, Phys. Rev. Lett. **108**, 216802 (2012).
[13] G. Tarnopolsky, A. J. Kruchkov, and A. Vishwanath, Phys. Rev. Lett. **122**, 106405 (2019).
[14] Y. Ren, Q. Gao, A. H. MacDonald, and Q. Niu, Phys. Rev. Lett. **126**, 016404 (2021).
[15] L. Balents, SciPost Phys. **7**, 48 (2019).
[16] Z.-X. Luo, C. Xu, and C.-M. Jian, Phys. Rev. B **104**, 035136 (2021).
[17] T. Kariyado and A. Vishwanath, Phys. Rev. Research **1**, 033076 (2019).
[18] M. Vogl, M. Rodriguez-Vega, and G. A. Fiete, Phys. Rev. B **101**, 235411 (2020).
[19] G. E. Topp, G. Jotzu, J. W. McIver, L. Xian, A. Rubio, and M. A. Sentef, Phys. Rev. Research **1**, 023031 (2019).
[20] Y. Zhang, Y. Gao, and D. Xiao, Phys. Rev. B **101**, 041410 (2020).
[21] J. M. B. Lopes dos Santos, N. M. R. Peres, and A. H. Castro Neto, Phys. Rev. B **86**, 155449 (2012).
[22] J. Liu, J. Liu, and X. Dai, Phys. Rev. B **99**, 155415 (2019).
[23] Q. Wu, J. Liu, Y. Guan, and O. V. Yazyev, Phys. Rev. Lett. **126**, 056401 (2021).
[24] D. Zhai and W. Yao, Phys. Rev. Lett. **125**, 266404 (2020).
[25] I. Yudhistira, N. Chakraborty, G. Sharma, D. Y. H. Ho, E. Laksmono, O. P. Sushkov, G. Vignale, and S. Adam, Phys. Rev. B **99**, 140302 (2019).
[26] M. Koshino, N. F. Q. Yuan, T. Koretsune, M. Ochi, K. Kuroki, and L. Fu, Phys. Rev. X **8**, 031087 (2018).
[27] J. Kang and O. Vafek, Phys. Rev. Lett. **122**, 246401 (2019).
[28] B. A. Bernevig, B. Lian, A. Cowsik, F. Xie, N. Regnault, and Z.-D. Song, Phys. Rev. B **103**, 205415 (2021).
[29] P. Potasz, M. Xie, and A. H. MacDonald, arXiv:2102.02256.
[30] Y. Da Liao, J. Kang, C. N. Breiø, X. Y. Xu, H.-Q. Wu, B. M. Andersen, R. M. Fernandes, and Z. Y. Meng, Phys. Rev. X **11**, 011014 (2021).
[31] X. Zhang, G. Pan, Y. Zhang, J. Kang, and Z. Y. Meng, Chin. Phys. Lett. **38**, 077305 (2021).
[32] J. Vahedi, R. Peters, A. Missaoui, A. Honecker, and G. T. de Laissardière, arXiv:2104.10694.

- [33] T. Soejima, D. E. Parker, N. Bultinck, J. Hauschild, and M. P. Zaletel, Phys. Rev. B **102**, 205111 (2020).
- [34] J. Kang and O. Vafek, Phys. Rev. B **102**, 035161 (2020).
- [35] N. Grandi, V. Juričić, I. S. Landea, and R. Soto-Garrido, JHEP **2021** (5), 123.
- [36] J. Gaa, G. Palle, R. M. Fernandes, and J. Schmalian, Phys. Rev. B **104**, 064109 (2021).
- [37] J. Wang, J. Cano, A. J. Millis, Z. Liu, and B. Yang, arXiv:2105.07491.
- [38] A. Parhizkar and V. Galitski, arXiv:2108.04252.
- [39] B. Han, H. Wang, and P. Ye, Phys. Rev. B **99**, 205120 (2019).
- [40] Z.-M. Huang, L. Li, J. Zhou, and H.-H. Zhang, Phys. Rev. B **99**, 155152 (2019).
- [41] J. Nissinen and G. E. Volovik, Phys. Rev. Research **1**, 023007 (2019).
- [42] Y. You and Y.-Z. You, Phys. Rev. B **93**, 245135 (2016).
- [43] M. O. Katanaev, Proceedings of the Steklov Institute of Mathematics **313**, 78–98 (2021).
- [44] T. Zhang, N. Regnault, B. A. Bernevig, X. Dai, and H. Weng, arXiv:2101.04934.
- [45] H. Ochoa and R. M. Fernandes, arXiv:2108.10342.
- [46] S. M. Davis and M. S. Foster, arXiv:2107.04047.
- [47] H. Kleinert, *Gauge Fields in Condensed Matter* (Gauge Fields in Condensed Matter - Volume 2 Pub: Clarendon Press, Oxford, 1885, 1989).
- [48] D. R. Hofstadter, Phys. Rev. B **14**, 2239 (1976).
- [49] J.-Q. Cai, Q.-Y. Yang, Z.-Y. Xue, M. Gong, G.-C. Guo, and Y. Hu, arXiv:1812.02610.
- [50] C. D. Beule, F. Dominguez, and P. Recher, arXiv:2107.04812.
- [51] M. Vozmediano, M. Katsnelson, and F. Guinea, Phys. Rep. **496**, 109 (2010).
- [52] A. Farjami, M. D. Horner, C. N. Self, Z. Papić, and J. K. Pachos, Phys. Rev. B **101**, 245116 (2020).
- [53] O. Golan, arXiv:2106.10897.
- [54] M. Gong, M. Lu, H. Liu, H. Jiang, Q.-F. Sun, and X. C. Xie, Phys. Rev. B **102**, 165425 (2020).
- [55] Q. Niu, D. J. Thouless, and Y.-S. Wu, Phys. Rev. B **31**, 3372 (1985).
- [56] Z.-D. Song, L. Elcoro, and B. A. Bernevig, Science **367**, 794 (2020).
- [57] L.-J. Zhai, S. Yin, and G.-Y. Huang, Phys. Rev. B **102**, 064206 (2020).
- [58] O. Boada, A. Celi, J. I. Latorre, and M. Lewenstein, NEW J PHYS **13**, 035002 (2011).
- [59] Y.-H. Zhang, D. Mao, Y. Cao, P. Jarillo-Herrero, and T. Senthil, Phys. Rev. B **99**, 075127 (2019).
- [60] C. Lv, R. Zhang, and Q. Zhou, arXiv:2106.02477.
- [61] M. Stålhammar, J. Larana-Aragon, L. Rødland, and F. K. Kunst, arXiv:2106.05030.
- [62] S.-X. Wang and S. Wan, arXiv:2108.08146.
- [63] G. Wagner, F. de Juan, and D. X. Nguyen, arXiv:1911.02028.
- [64] M. I. Katsnelson and M. F. Prokhorova, Phys. Rev. B **77**, 205424 (2008).
- [65] X. Chen, Z.-C. Gu, and X.-G. Wen, Phys. Rev. B **82**, 155138 (2010).
- [66] Z. Liu, E. J. Bergholtz, and J. C. Budich, arXiv:2108.10327.
- [67] J. N. Leaw, H.-K. Tang, M. Trushin, F. F. Assaad, and S. Adam, PNAS **116**, 26431 (2019).
- [68] Y. Aharonov and J. Anandan, Phys. Rev. Lett. **58**, 1593 (1987).
- [69] G. E. Topp, C. J. Eckhardt, D. M. Kennes, M. A. Sentef, and P. Törmä, arXiv:2103.04967.
- [70] S. Yao, Z. Yan, and Z. Wang, Phys. Rev. B **96**, 195303 (2017).
- [71] D. J. Thouless, Phys. Rev. B **27**, 6083 (1983).
- [72] S. Bagchi, H. T. Johnson, and H. B. Chew, Phys. Rev. B **101**, 054109 (2020).
- [73] Z. Fedorova, H. Qiu, S. Linden, and J. Kroha, Nat Comm **11**, 3758 (2020).
- [74] Ryder and LewisH, *Quantum field theory* (Quantum field theory, 1985).
- [75] B. Mera and T. Ozawa, arXiv:2107.09039.
- [76] M. Yoshii, S. Kitamura, and T. Morimoto, arXiv:2105.05654.
- [77] Q.-B. Zeng, Y.-B. Yang, and Y. Xu, Phys. Rev. B **101**, 020201 (2020).
- [78] H. Huang and F. Liu, Phys. Rev. Lett. **121**, 126401 (2018).
- [79] C.-B. Hua, Z.-R. Liu, T. Peng, R. Chen, D.-H. Xu, and B. Zhou, arXiv:2107.01439.
- [80] Z. Gong, Y. Ashida, K. Kawabata, K. Takasan, S. Higashikawa, and M. Ueda, Phys. Rev. X **8**, 031079 (2018).
- [81] Y.-S. Hu, Y.-R. Ding, J. Zhang, Z.-Q. Zhang, and C.-Z. Chen, arXiv:2106.00422.
- [82] H. Liu, Z. Su, Z.-Q. Zhang, and H. Jiang, Chin. Phys. B. **29**, 050502 (2020).
- [83] D. C. Brody, J PHYS A-MATH THEOR **47**, 035305 (2013).
- [84] H. Wu and J.-H. An, Phys. Rev. B **102**, 041119 (2020).
- [85] A. H. Castro Neto, F. Guinea, N. M. R. Peres, K. S. Novoselov, and A. K. Geim, Rev. Mod. Phys. **81**, 109 (2009).
- [86] C. C. Barros, EPJ C **42**, 119 (2005).